Ultrafast third-harmonic generation from textured aluminum nitride–sapphire interfaces

D. S. Stoker,[1,2,*] J. Baek,[3,2] W. Wang,[3,2,†] D. Kovar,[4,2] M. F. Becker,[3,2] and J. W. Keto[5,2]

[1]*Department of Physics, The University of Texas at Austin, 1 University Station C1600, Austin, Texas 78712-0264, USA*

[2]*Center for Nano- and Molecular Science and Technology and the Texas Materials Institute, The University of Texas at Austin, Building ETC, Room 8.102, Campus Mail Code C2201, Austin, Texas 78712-1063, USA*

[3]*Electrical and Computer Engineering, The University of Texas at Austin, 1 University Station C0803, Austin, Texas 78712-0240, USA*

[4]*Mechanical Engineering Department, The University of Texas at Austin, 1 University Station C2200, Austin, Texas 78712-0292, USA*

[5]*Department of Physics, The University of Texas at Austin, 1 University Station C1600, Austin, Texas 78712-0264, USA*

(Received 8 December 2005; revised manuscript received 11 March 2006; published 11 May 2006)

We measured and modeled third-harmonic generation (THG) from an AlN thin film on sapphire using a time-domain approach appropriate for ultrafast lasers. Second-harmonic measurements indicated that polycrystalline AlN contains long-range crystal texture. An interface model for third-harmonic generation enabled an analytical representation of scanning THG (z-scan) experiments. Using it and accounting for Fresnel reflections, we measured the AlN–sapphire susceptibility ratio and estimated the susceptibility for aluminum nitride, $\chi^{(3)}_{xxxx}(3\omega;\omega,\omega,\omega)=1.52\pm0.25\times10^{-13}$ esu. The third-harmonic (TH) spectrum strongly depended on the laser focus position and sample thickness. The amplitude and phase of the frequency-domain interference were fit to the Fourier transform of the calculated time-domain field to improve the accuracy of several experimental parameters. We verified that the model works well for explaining TH signal amplitudes and spectral phase. Some anomalous features in the TH spectrum were observed, which we attributed to nonparaxial effects.

DOI: 10.1103/PhysRevA.73.053812 PACS number(s): 42.65.Ky, 42.65.Re, 78.20.−e, 78.47.+p

I. INTRODUCTION

The z-scan is a straightforward and sensitive method for analyzing nonlinear optical materials using a focused laser. Since it measures how a nonlinear signal changes as a function of the input focus position, it is a fairly direct measure of the nonlinear susceptibility. Applied to degenerate four-wave mixing (DFWM), the z-scan has become a useful tool for characterizing optical switches and other nonlinear Kerr effects [1]. The well-developed formalism permits the measurement of both the real and imaginary parts of the nonlinear susceptibility. Recently, the z-scan principle has been broadened to include other nonlinear optical effects and has been introduced to third-harmonic generation in optical solids and thin liquid layers [2–7]. In this paper, third-harmonic (TH) z-scans of an AlN film were used to determine the film's third-order susceptibility $\chi^{(3)}$.

AlN is an interesting material, technologically, and is widely utilized in optoelectronic devices [8,9]. The primary feature of AlN is a large band gap, which makes it amenable to generating a TH field in the ultraviolet (UV) [10,11]. In bulk crystalline form, it does not have a large susceptibility, but it could serve as a passive matrix material in a nanocomposite, containing an active material with a larger nonlinear coefficient [12]. In that case AlN could serve as a passive matrix in UV and ultrafast light modulators or in other nonlinear devices requiring short wavelength operation [13,14]. In a recent report, AlN films generated by pulsed laser deposition (PLD) were shown to contain nanotexturing [15].

Ultrafast lasers have been utilized to perform TH generation (THG) microscopy [4,5,16–18]. These experiments used tightly focused beams, which have Rayleigh ranges shorter than the group velocity walk-off length. Their experimental model relies on focusing effects stemming from the Guoy phase shift and neglects group-velocity mismatch of the fundamental and harmonic pulses [19,20]. In a recent article, we showed that THG using focused ultrafast lasers, in which the Rayleigh range is longer than the group velocity walk-off, is not affected by the Guoy phase shift. In that article we identified group-velocity mismatch (GVM) and phase-velocity mismatch as the important parameters responsible for past observations of interface-sensitive THG [7].

Even with the theoretical complications imposed by focusing, work by Barille *et al.* and Petrov *et al.* showed that tightly focused lasers can be used to make accurate susceptibility measurements of liquid and solid thin films [5,12]. Furthermore, a tight focus allows for spatial discrimination of nonlinearities in inhomogeneous materials [4]. Despite the successes in quantifying THG susceptibilities, there are a few notable deficiencies: tight focusing produces an asymmetric z-scan shape which is not well modeled by a paraxial beam formula [4,5], numerical techniques were required to evaluate the phase matching integrals [5,12], and many of the studies were carried out in untextured or amorphous samples, which did not require consideration of the tensor nature of the susceptibility [5,12]. In this paper, we demonstrate that using a slightly lower numerical aperture offers at least two important advantages: an accurate representation of the z-scan shape and an analytical approach to calculating the

*Electronic address: stoker@mail.utexas.edu

†Present address: AKT America, Inc. An Applied Materials Company, 3101 Scott Blvd., M/S 9106 PO Box 58039 Santa Clara, CA 95054.

susceptibility. Furthermore, we supplement the previous reports with a systematic method for dealing with group velocity walk-off in third-harmonic generation, which when analyzed in the time domain allows for the calculation of the time-dependent phase of the radiated TH field. The phase sensitivity is carried throughout our analysis, and we will show it can be measured from the TH spectrum [7].

In the absence of phase matching, THG originates from the boundaries of bulk nonlinear media. At the dielectric boundary, interruption of phase matching causes an interface-localized growth of the TH field. THG from interfaces is distinct from surface second-harmonic generation (SHG), which is a sensitivity to angular momentum conservation [21]. More applicable is Kleinman and Miller's description of harmonic generation in isotropic, phase-mismatched media [22]. They described a surface response that is not exclusive to second-order processes and is applicable to cw THG experiments. However, ultrafast pulses are only overlapped for a distance smaller than the group-velocity walk-off length. Group-velocity walk-off is practically universal when near-infrared (NIR) pulses are used, since the third harmonic is near the band edge of many optical materials such as quartz, sapphire, fused silica, and LiF. In a recent experiment, 130-nm pulses from the interfaces of a MgF_2 slab were directly observed [23].

Measuring the third-order susceptibility $\chi^{(3)}(3\omega;\omega,\omega,\omega)$ of AlN requires knowing the relative third-harmonic response of the film and substrate, but other factors in addition to susceptibility contribute to a measured third-harmonic signal. Previously, tightly focused experiments in nearly or exactly index-matched media could neglect reflections, but this is not possible near interfaces with a larger index mismatch, such as an AlN–sapphire interface [4,5]. We performed independent measurements of the reflection losses and phase matching in the film and substrate, the rotational (azimuthal) harmonic dependence determined the macroscopic crystal ordering (texture) and we accounted for the coherent interaction of the film and substrate fields. Knowing all these parameters is a requirement for properly estimating the AlN/Al_2O_3 susceptibility ratio [24].

This paper is divided into several sections: Sec. II gives a condensed account of pulse propagation theory and its relation to harmonic generation. Section III describes the deposition and characterization of the AlN film and the azimuthal dependence of the nonlinear optical response at second and third order. Then, Sec. IV describes the origin of interface sensitivity using a pulsed plane-wave model and linear material properties measured for the AlN–sapphire system. The interface approach is extended to focused z-scan measurements of AlN in Sec. V by modifying the plane-wave approach of the previous section. Calculation of the TH susceptibility is followed by an analysis of the THG spectrum in Sec. VI.

II. THG WITH GROUP-VELOCITY MISMATCH

The relevant equations are derived by including the pulse dispersion in the nonlinear wave equation. An analysis of THG including GVM was recently reported by Tasgal and Band [25]. For details, we encourage the reader to consult their article, which includes both transverse and longitudinal effects. The main result is derived briefly in this section.

The laser pulses propagate along the z axis, and the propagation is assumed to be independent of x,y. The effects of focusing a Gaussian beam are described in Sec. V. Therefore, the basic starting point is the one-dimensional wave equation with linear and nonlinear driving terms,

$$\frac{\partial^2}{\partial t^2}\tilde{E}_i(z,t) - \frac{1}{c^2}\frac{\partial^2}{\partial z^2}\tilde{E}_i(z,t) = \frac{-4\pi}{c^2}\frac{\partial^2 \tilde{P}_i}{\partial t^2}, \tag{1a}$$

$$\tilde{P}_i = \tilde{P}_i^{\mathrm{NL}} + \tilde{P}_i^{(1)}. \tag{1b}$$

Energy transfer between the fundamental and harmonic fields occurs through the nonlinear polarization $\tilde{P}_i^{\mathrm{NL}}$, while the linear polarization $\tilde{P}_i^{(1)}$ determines how each pulse propagates. Growth of each of the nonlinear polarization components occurs with an efficiency determined by the product of the third-order nonlinear susceptibility and a triple product of the propagating fields,

$$\tilde{P}_3^{\mathrm{NL}} = \chi^{(3)} \vdots \tilde{E}_1\tilde{E}_1\tilde{E}_1, \tag{2a}$$

$$\tilde{P}_1^{\mathrm{NL}} = 3\chi^{(3)} \vdots \tilde{E}_3\tilde{E}_1^*\tilde{E}_1^*. \tag{2b}$$

In our approach, we neglected higher-order contributions to the TH polarization.

Computing the Fourier transform of $\tilde{P}_i^{(1)}$, in accordance with the derivation of the parabolic wave equation, leaves dispersion of the ω_i field described by $\omega^2\chi^{(1)}(\omega)$ [26], which expands to

$$\omega^2\chi(\omega) \approx \omega_i^2\chi(\omega_i) + \frac{d}{d\omega}[\omega^2\chi(\omega)]\Big|_{\omega=\omega_i} \times (\omega-\omega_i) + \cdots. \tag{3}$$

The linear susceptibility $\chi^{(1)}$ can be rewritten in terms of the propagation constant $k(\omega)=k(\omega_i)+\left[\frac{dk}{d\omega}\right]\Big|_{\omega=\omega_i}\times(\omega-\omega_i)+\cdots$, where ω_i refers to the fundamental or harmonic field. The result, using the relationship $k^2(\omega)=(\omega^2/c^2)[1+\chi(\omega)]$ and assuming that the envelope of the pulse is slowly varying, implies that the ω_i field freely propagates according to

$$\frac{\partial \tilde{E}_i(z,t)}{\partial z} + \frac{1}{v_{g,i}}\frac{\partial \tilde{E}_i(z,t)}{\partial t} = \frac{-4\pi}{c^2}\frac{\partial^2 \tilde{P}_i^{\mathrm{NL}}(z,t)}{\partial t^2}. \tag{4}$$

Equation (4) can be rewritten in terms of reduced time with a change of variables $\eta_i \equiv t - z/v_{g,i}$ and $z' \equiv z$, resulting in the simplified form

$$\frac{\partial \tilde{E}_i(z',\eta_i)}{\partial z'} = \frac{-4\pi}{c^2}\frac{\partial^2 \tilde{P}_i^{\mathrm{NL}}(z',\eta_i)}{\partial \eta_i^2}. \tag{5}$$

Equation (5) describes third-harmonic generation in the rest frame of the TH pulse. In the TH reference frame, the nonlinear polarization moves with the group velocity of the ω_1 pulse $v_{g,1}$, which is faster by $\frac{1}{\Delta\beta}$. We assumed the fields do not attenuate and there are no resonances near the fundamen-

TABLE I. Sellmeier fit parameters.

Material	a	b	c
Al_2O_3[a]	0.898	2.172	0.092
AlN	1.4(2)[b]	2.7(2)	0.135(4)

[a]The sapphire index error is negligibly small and not stated.
[b]Digits in parentheses indicate the error in the last digit, $1.4(2) \equiv 1.4 \pm 0.2$.

tal or third-harmonic wavelengths. For these reasons, we consider only the real value of the linear susceptibility. We also assumed $\chi^{(3)}$ is isotropic, which we justify in Sec. III.

Group-velocity effects have been used to treat picosecond SHG, but pulse walk-off was assumed not to occur [27]. In femtosecond SHG pulse walk-off does occur [28]. Recent work has shown that THG is more susceptible to walk-off because of a larger dispersion and shorter pulse lengths [7,25,29]. Additionally, for a given group-velocity mismatch, the pulse length τ_p of the TH is shorter, causing walk-off to occur more rapidly for THG. In typical optical materials, when using a NIR pump, the third harmonic of the fundamental wavelength $\frac{\lambda_0}{3}$ is at the band edge, where $\frac{dn}{d\lambda}$ is large.

III. SAMPLE PREPARATION

A. AlN film deposition

We used PLD to deposit the AlN thin film. The ablation source was a 248-nm Kr:F excimer laser, pulsed at 30 Hz, at 150 mJ pulse^{-1}. The laser was focused to ~ 0.03 cm^2 at the AlN target surface, in a 0.58-mTorr N_2 atmosphere. The plasma plume was directed at a nearby (5-cm), 330-μm-thick sapphire (0001) substrate, held at 800 °C, which allowed the plasma constituents to recombine and form a film. During the 30 min deposition, the laser focus moved in a circle at 0.5 Hz, to increase film uniformity. Preparing films in this way produced a material with a slightly wedged shape, of average thickness of 306.3 nm, but other material properties such as density and surface roughness are superior to evaporation-based methods [30].

B. Linear optical characterization

Preliminary linear optical analysis determined phase matching parameters, group delay parameters, and Fresnel reflection losses. Because the PLD technique produced films with a wedge shape, the measurements were done on just a small, ~ 1 mm^2 total area, to improve accuracy. The linear transmission spectrum contained interference fringes, which were used to determine the linear refractive index, absorptiveness, and film thickness [30]. The calculated index of refraction was fit by a Sellmeier equation

$$n(\lambda) = \sqrt{a + \frac{b\lambda^2}{(\lambda^2 - c^2)}}. \tag{6}$$

The fitted parameters for both the film and the sapphire substrate are shown in Table I.

TABLE II. Fresnel factors.

$\mathcal{F}_i^j(\omega)$	Value[a]	Description	Method
$\mathcal{F}_1^B$	0.961 (1)	Pump transmission air–sapphire	$\sqrt{1-\frac{[1-n(\lambda_0)]^2}{[1+n(\lambda_0)]^2}}$
$\mathcal{F}_3^B$	0.956 (1)	TH transmission air–sapphire	$\sqrt{1-\frac{[1-n(\lambda_0/3)]^2}{[1+n(\lambda_0/3)]^2}}$
$\mathcal{F}_1^{TF}$	0.899 (3)	Pump transmission through AlN film	$\frac{\mathcal{F}_1^T}{\mathcal{F}_1^B}$
$\mathcal{F}_3^{TF}$	0.806 (3)	TH transmission through AlN film	$\frac{\mathcal{F}_3^T}{\mathcal{F}_3^B}$

[a]Note that the stated errors are 1σ standard deviations.

Nonlinear analysis requires the reflection loss at each interface to be distinguished from the total loss of the film and substrate material. The total optical transmission of the pump field is determined by the product of the Fresnel transmission factors for the wave amplitudes in the bulk and the thin film,

$$\mathcal{F}_1^T = \mathcal{F}_1^B \mathcal{F}_1^{TF}. \tag{7}$$

The field transmission factor $\mathcal{F}_i^B$ defines the ith field's transmission through a bulklike interface. The field transmission factor $\mathcal{F}_i^{TF}$ defines transmission at the thin-film, Al_2O_3–AlN interface. Each of the interface coefficients contributes separately to the nonlinear, thin-film equations and is assumed to be real-valued, since both the third harmonic and fundamental are far from the band edge. The individual Fresnel coefficients for the sapphire–air interface were calculated directly from the indices of refraction. However, to account for multiple reflections in the film, we inferred the thin-film coefficients from the measured transmission using Eq. (7). The Fresnel factors relevant for nonlinear analysis are summarized in Table II.

C. Characterization of texture

Plasma growth of AlN is known to produce texturing of the crystallites in the film [8–10]. An attempt to quantify the long-range ordering of the crystal grains using nonlinear optical techniques has been reported [14]. What causes texturing is not fully understood, but is thought to correspond to unique conditions during growth. We confirmed that our film has texture by measuring the rotational dependence of SHG.

Rotational analysis of the AlN film texture was achieved by recording the intensity of the second harmonic as the sample was rotated about the surface normal. A Ti:sapphire oscillator (30 nm bandwidth, 87 MHz repetition, 600 mW average power) was focused at the AlN film interface to a waist diameter of 15 μm. The emitted SH photons were filtered by a Schott glass color filter and directed into a spectrograph, where they were further filtered and spectrally resolved. For each angular position, a spectrum was recorded and integrated to determine the radiated SH power. A Glan-Thompson polarization analyzer was used to separate the SH into s and p components.

Since we observe SHG, we know there is some macroscopic ordering to the wurzite microcrystals; the crystals are

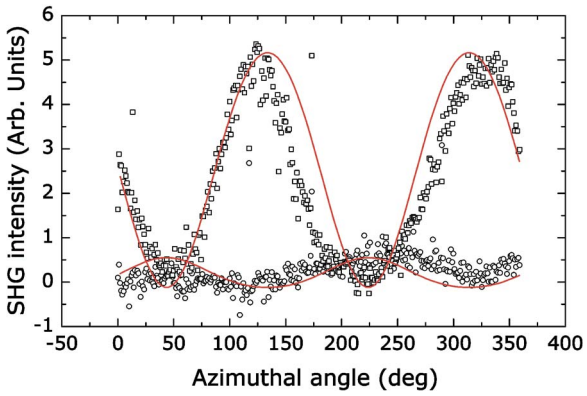

FIG. 1. (Color online) SHG measured from AlN in both polarization orientations $p_{in} \rightarrow p_{out}$ (□) and $p_{in} \rightarrow s_{out}$ (○). Shown as solid lines are independent calculations of the rotational anisotropy of a hexagonal (C_{6v}^4) crystal, one for each of the x- and y-polarized emissions under x-polarized excitation. Including a rotation about the x axis by $\pi/10$ rad produced the best fit to the data and indicates that the crystal axis of the aluminum nitride crystals grows with a small tilt, compared to the underlying sapphire.

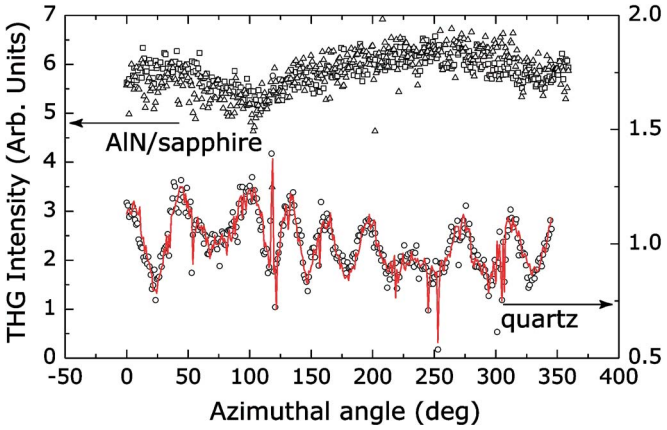

FIG. 2. (Color online) THG from AlN, measured in both polarization orientations $p_{in} \rightarrow p_{out}$ (□) and $p_{in} \rightarrow s_{out}$ (△). For comparison, the measurement was repeated on a 100−μm-thick piece of z-cut quartz. Two azimuthal measurements of $p_{in} \rightarrow (s+p)_{out}$ THG are shown. The scatter data (○) correspond to shorter integration. The line through it is the same measurement, just taken with longer exposure.

so small that randomly oriented grains are essentially amorphous and SHG inactive [14]. Generally, AlN films produced by PLD show a variable grain size that increases as the distance from the substrate increases, from a few nanometers near the sapphire interface, up to 100 nm for several-micron-thick films [10]. For SHG, all of the signal originated in the AlN film; the sapphire substrate with (0001) orientation has no SHG response.

To model the SHG rotational anisotropy, we computed an effective, laboratory-frame tensor from the ideal, hexagonal C_{6v}^4 (wurzite) crystal aligned with the z-axis of the substrate, as in previous studies of GaN thin films [28]. The best fit to the experimental data was found by incorporating a small crystal tilt (less than $\pi/10$ rad) about the x axis. Smaller tilts decreased the magnitude of the calculated rotational contrast without altering the periodicity. Independent calculations of both the s_{out} and p_{out} SHG signal are shown with the experimental data in Fig. 1. Based on the fit to the data, our sample texture is close to an ideal wurzite crystal of aluminum nitride, with the crystal axis tilted slightly with respect to the sapphire substrate crystal axis. The fit is not expected to be perfect, since texturing only approximates an ideal crystal. Additional error in the fit originates from the laser focus not being located at the rotational fixed point; different angles probe different portions of the film.

It is known that THG is sensitive to material structure, so we repeated the rotational measurement for THG at the AlN–sapphire interface and show the result in Fig. 2 [2,31]. Rotational THG could not resolve any $\chi^{(3)}$ anisotropy, neither in the bare substrate nor in the film. The individual $p_{in} \rightarrow p_{out}$ and $p_{in} \rightarrow s_{out}$ components of THG in the AlN film are essentially identical. The azimuthal response of quartz demonstrates THG has structural sensitivity; the overall periodicity matches the greater periodicity expected for THG. The quartz data in Fig. 2 indicate a sensitivity to surface defects, demonstrated by the repeatable distortions of the harmonic signal. When the quartz measurements were repeated, the fine details at 55°, 120°, 250°, and 300° were duplicated.

IV. THG FROM AlN–SAPPHIRE INTERFACES

A previous paper showed that the interface THG arises from an interplay between group velocity and phase mismatching [7]. These coherent effects are always accompanied by a large, incoherent discontinuity in $\chi^{(3)}$ which initiates the signal growth from a region determined by the coherence length L_c.

Plotting the integral of Eq. (5) over a single slab of material as a function of time is a way to characterize the origin of the nonlinear response. The third-harmonic field has temporal dispersion, due to GVM, so a particular time in the third-harmonic output is generated by a particular portion of the nonlinear medium. In the time domain we calculate that two unbroadened pulses will emerge, separated by a time corresponding to the nonlinear medium (slab) thickness, indicating that only the material in the vicinity of the interfaces generates a third harmonic.

First, we treat the interface THG response assuming a Gaussian-pulsed, collimated beam. We begin by deriving an analytical solution for a single slab, which we use later when approximating boundaries as a superposition of two slabs of dissimilar material. Since AlN thin films grown on Al_2O_3 are the interest of this paper, many of the details of that system are provided in this section in parallel with the theoretical description. We also found it is convenient to adopt ultrafast units for the parameters listed in Table III [28].

The oscillating fundamental field

$$\tilde{E}_1(z,t) = \tilde{A}_1(z,t)e^{i(\omega t - k_1 z)} \tag{8}$$

is proportional to a slowly varying complex amplitude $\tilde{A}_1(z,t)$. As written, Eq. (8) applies to any space-time pulse type, be it Gaussian or some arbitrary shape. Substituting $\tilde{E}_1(z,t)$ into Eq. (5) and canceling common terms gives

TABLE III. Ultrafast values.

Parameter	Value	Units	Significance
Γ	0.00141	fs^{-2}	Gaussian time parameter
c	0.3	$\mu m\ fs^{-1}$	Vacuum phase velocity
$\Delta\lambda$	0.03	μm	Pump bandwidth
λ_0	0.800	μm	Pump centroid[a]

[a]Nominal value. Experimental values varied ±5 nm.

$$\frac{d\tilde{A}_3}{dz} = \frac{i2\pi\omega_3^2\chi^{(3)}\tilde{A}_1^3(z,t-\Delta\beta z)e^{i\Delta kz}}{k_3c^2}. \tag{9}$$

The group delay term $\Delta\beta z$ in Eq. (9) has a minus sign, indicating that the nonlinear driving term will continuously travel ahead of the harmonic field. Equation (9) must be evaluated numerically for a Gaussian-focused beam, but has an analytical solution for plane-wave pulses.

Phase matching for third-harmonic generation is introduced in Eq. (9) as $\Delta k = 3k_1 - k_3$. The phase mismatch Δk is a measure of linear dispersion in an optical material, seen by rewriting it as $\Delta k = 2\pi q\Delta n/\lambda_0$, and accounts for the relative phase of the ω and 3ω fields Δkz as they propagate a distance z through a material. When $\Delta k \neq 0$, there is a coherent transfer of energy between the ω and 3ω fields over a characteristic distance $L_c = 2\pi/\Delta k$.

Equation (9) is integrated over the nonlinear material length to find the generated third-harmonic field as a function of time at the exit surface,

$$\tilde{A}_3(t) = \int_{z_i}^{z_f} dz \frac{i2\pi\omega_3^2\chi^{(3)}\tilde{A}_1^3(z,t-\Delta\beta z)e^{i\Delta kz}}{k_3c^2}. \tag{10}$$

Taking the limit as $\Delta\beta \to 0$, $\tilde{A}_3(t)$ reduces to the case describing focusing's effect on THG in gases [19,20,32].

If $\Delta k \neq 0$, varying the thickness of a nonlinear medium brings an oscillation of nonlinear signal intensity [33]. Extending this Maker fringe model to ultrafast pulses, Angerer *et al.* showed the SHG loses phase coherence in thick samples and that the SHG signal deviates from the cw case [28]. Ultrafast THG displays an even more pronounced deviation, because of the larger dispersion between the fundamental and harmonic wavelengths. We integrated Eq. (10) for different pulse lengths, assuming an unfocused laser each time, and plotted the TH intensity as a function of material thickness in Fig. 3.

There is a strong effect of pulse length on THG. Based on Fig. 3, two *regimes* are identified. The first, relevant to long pulses, is identified by periodic energy transport over large distances. The short pulse case is easily differentiated in thicker materials, whereby little coherence exists between the harmonic and pump fields. The thinnest optical materials maintain a cw response for any pulse length, because there is not enough material for pulse walk-off to occur.

It appears as though the sensitivity of the TH field to small changes in the thickness of the bulk material disappears in thick materials, when using an ultrafast laser. This is true if only the TH intensity is measured. In fact, the sensitivity to the thickness parameter is not lost: it is maintained by the phase of the TH field. To show how to retain the sensitivity to material thickness, the following analysis includes the phase of the TH pulse.

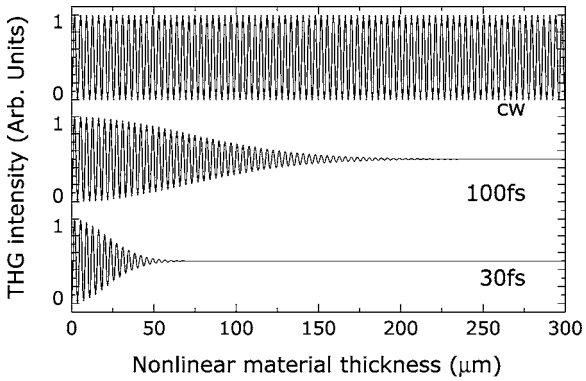

FIG. 3. Calculated transmitted third-harmonic intensity as a function of Al_2O_3 thickness. Three different laser pulses plotted for reference. The cw laser has the longest $1/e$ damping distance (∞) for the Maker fringes. The 100-fs laser and 30-fs laser pulses damp over a much shorter distance, because of GVM effects. The high-frequency oscillations are spaced by the coherence length $L_c = 3.65\ \mu m$. This calculation assumes an unfocused beam.

If the $\tilde{A}_1$ field is collimated and interacts with a dispersive optical element, it generates a time-dependent, harmonic field

$$\tilde{A}_3(t) = \frac{i2\pi\omega_3^2\chi^{(3)}A_1^3}{k_3c^2}\int_{z_i}^{z_f} dz e^{-3\Gamma(t-\Delta\beta z)^2}e^{i\Delta kz}. \tag{11}$$

To evaluate the integral we assumed

$$\tilde{A}_1^3(z,t) = A_1^3 e^{-3\Gamma(t-\Delta\beta z)^2} \tag{12}$$

and $\chi^{(3)}$ is spatially nonvarying and defined by a stepwise increase in the magnitude, an assumption common to other reports [4,19,20,25]. Equation (11) can be separated into real and imaginary parts, and integrated. Doing so yields

$$\tilde{A}_3(t) = \frac{i2\pi\omega_3^2\chi^{(3)}A_1^3\sqrt{\pi}}{k_3c^2 2\sqrt{3\Gamma}\Delta\beta}\left\{e^{-\Delta k(\Delta k - i12t\Gamma\Delta\beta)/12\Gamma\Delta\beta^2} \times \left(-\mathrm{erf}\left[\frac{i\Delta k + 6\Gamma\Delta\beta(t - z_f\Delta\beta)}{2\sqrt{3\Gamma}\Delta\beta}\right] + \mathrm{erf}\left[\frac{i\Delta k + 6\Gamma\Delta\beta(t - z_i\Delta\beta)}{2\sqrt{3\Gamma}\Delta\beta}\right]\right)\right\}. \tag{13}$$

The variables

$$\zeta_k \equiv \frac{\Delta k}{\xi^{1/2}}, \tag{14a}$$

$$\zeta_t \equiv t\sqrt{3\Gamma}, \tag{14b}$$

$$\xi \equiv 12\Gamma\Delta\beta^2 \tag{14c}$$

simplify the form of Eq. (13) to

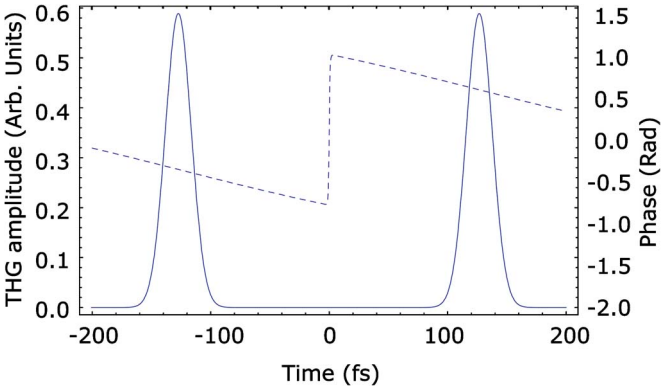

FIG. 4. (Color online) Transmitted third-harmonic field strength. Also plotted as a dashed line is the phase, which shows that for an initially unchirped pulse, the harmonic pulse that is generated is linearly chirped. The calculation assumes 330 μm of c-plane sapphire, which corresponds to the substrate thickness in our samples. Calculations for slightly different thicknesses cause the phase jump at $t=0$ to change, but the amplitude to remain the same.

$$\tilde{A}_3(t) \propto \sqrt{\frac{\pi}{\xi}} e^{(-\zeta_k^2+2i\zeta_k\zeta_t)} \left\{ \mathrm{erf}\left[\zeta_t + \left(i\zeta_k - \frac{z_i \xi^{1/2}}{2} \right) \right] - \mathrm{erf}\left[\zeta_t + \left(i\zeta_k - \frac{z_f \xi^{1/2}}{2} \right) \right] \right\}. \quad (15)$$

The absolute value of Eq. (13) or (15) describes the time-dependent TH pulse amplitude, and the angle describes its phase. Each is plotted in Fig. 4. The TH field consists of a pair of pulses, which are separated in time. GVM introduces a chirp to each pulse. The jump in the relative phase of the two pulses is a manifestation of sensitivity to material thickness and is the phase analog of the thickness-dependent intensity oscillations of a cw laser. The temporal description of THG provides clear evidence of the interface response, because temporal dispersion identifies a particular time with a particular point in the material.

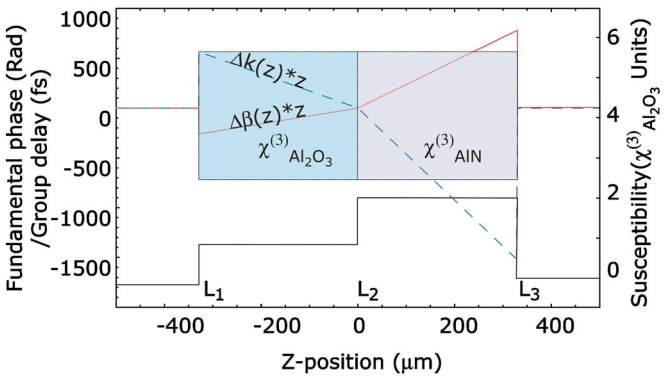

FIG. 5. (Color online) Shown here are both the group delay $\Delta\beta z$ and phase $\Delta k z$ for the two-slab model. These continuous parameters describe the z dependence of the entire material's dispersion and can be inserted into Eq. (15) to find the time-dependent radiated harmonic field due to all material interfaces. The interface between the two slabs is placed at $z=0$ to prevent any discontinuities in the group delay $\Delta\beta z$.

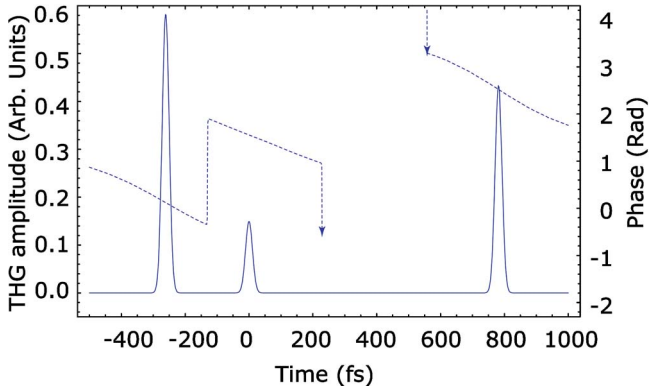

FIG. 6. (Color online) Shown here is the calculated time-dependent TH field, radiated from the model system in Fig. 5. Adding group delay and phase changes at the dielectric boundary affects both pulse separation and pulse magnitude. At the AlN–Al_2O_3 interface, there is a partial suppression of TH resulting from the vector addition of the amplitude and phase. The time-dependent phase is also plotted. Between $t=0$ and $t=775$ fs pulses, the phase change is rapid, with a linear slope of ~ -2.0 rad/fs.

The TH response is initiated by a discontinuity in $\chi^{(3)}$, but the magnitude of the generated field depends on abrupt changes in any of $\Upsilon=\{\Delta k, \Delta\beta, \chi^{(3)}\}$ at an interface. Table IV lists these values for AlN, Al_2O_3, and SiO_2. For multilayered materials, it is important to take care when introducing the inverse group-velocity mismatch $\Delta\beta$ and phase mismatch Δk into the z integral in Eq. (11). Otherwise, the group delay $\Delta\beta z$ and phase $\Delta k z$ will be unphysically discontinuous.

To illustrate the effect of changing the Υ parameters in multilayered materials, we calculated the time-dependent TH response of a thick slab of Al_2O_3 adjacent to an equally thick slab of AlN. There are now three interfaces: air–sapphire, sapphire–AlN, and AlN–air. The group delay and phase as a function of position in the material are shown in Fig. 5. We placed the interface at $z=0$ to prevent discontinuities in the group delay[1].

The TH field generated in the two-slab material was calculated using Eq. (15) twice: once for the Al_2O_3 slab and once for the AlN slab. The two solutions overlap at $t=0$ and add coherently. There are now three generated TH pulses. Both the amplitude and phase are plotted in Fig. 6. The jump in the phase between the pulses generated at each interface is again visible. Between the pulse from the sapphire–AlN interface and AlN–air interface, the phase cycles through 2π of phase many times. If a cw field were propagating through the same thickness of AlN, the fundamental and harmonic fields would oscillate in and out of phase as many times the phase cycles through 2π.

As a comparison, the time-dependent third-harmonic field, due solely to changes in $\Delta\beta$ and Δk, was calculated. We assumed the dispersion in Fig. 5, using the parameters in Table IV, but assumed no change in the nonlinear susceptibility at the sapphire–AlN interface. We calculated no change

[1]If a material interface at position z_i is encountered, a change in the inverse group-velocity mismatch $\Delta\beta$ for $z_i \neq 0$ causes an unphysical discontinuity in the group delay $\Delta\beta z_i$ [36].

TABLE IV. Relevant interface parameters.

Υ	Al_2O_3	AlN	SiO_2	Units
Δk	−1.72	−4.6(6)	−1.288	μm^{-1}
$\Delta\beta$	0.79	2.3(5)	0.5774	fs μm^{-1}

for the air–sapphire pulse and a decrease by a factor of 2 of the AlN–air interface. However, the pulse from the sapphire–AlN interface is *larger* by a factor of 2.5. When there is no change in both the susceptibility and Δk, but $\Delta\beta$ was allowed to vary, a smaller pulse by one order of magnitude was calculated. Based on the simulations of varying the individual Υ parameters, we conclude that all of them have significant contributions to THG from interfaces.

Ultrashort pulses generate TH differently, compared to long pulses, whereby long-range effects have dominated and were noted in earlier articles [20,32]. The phase mismatch and group-velocity mismatch inhibit the growth of TH radiation from the bulk, but within a coherence length of an abrupt change in the value of the susceptibility a TH field is generated. The magnitude of the fields generated in each material near the interface strongly depends on the phase matching factor Δk. As shown in Fig. 3, thin materials display Maker fringes, but thicker bulk optics do not. Thickness information is kept in the relative phase of the pulses generated at the entrance and exit interfaces of a slab of material. The analysis of multilayered materials also indicated that the phase of the TH fields strongly impacts how pulses will superimpose. Though the two-slab model assumes that the AlN has a thickness comparable to the substrate, the response of the 300-nm film is obtained using the same mathematics. In a film, the pulse located at the $t=775$ fs in Fig. 6 will overlap temporally and interfere with the $t=0$ pulse. Treating the thin film as a limiting case of a slab provides insight into the TH material response using ultrafast pulses.

V. Z-SCAN MEASUREMENTS OF INTERFACES

The treatment of Sec. IV demonstrated that TH pulses originate from nonlinear material boundaries. In a two-slab material, the pulses at the shared interface add coherently in time to give three pulses. Accordingly, THG from the AlN–sapphire sample is reduced to THG from three interfaces: air–sapphire, sapphire–AlN, and AlN–air. In a slow detector, the sum of the pulses is measured, so there is no information about individual interfaces. In theory, each pulse could be sampled using an ultrafast or pump-probe technique, but the z-scan is a more convenient technique of isolating the pulse from an individual interface. In this section, we show how the interface model of ultrafast THG can be used to model z-scans.

A. Model

The pulsed plane-wave approximation made in Eq. (15) is applicable to z-scan measurements that use focused ultrafast pulses. Because growth of the $\tilde{E}_3$ field turns off immediately after the $\tilde{E}_1$ field enters the bulk of the material, all the relevant information about the $\tilde{E}_1$ field is located right at the material interface. Consequently, if a focused laser is scanned through a dielectric interface, the THG signal will scale like the cube of the intensity of the fundamental field at the interface.

The change in the beam diameter varies slowly over the region generating the third-harmonic signal when ultrafast pulses are used. According to the arguments in Sec. IV, this distance is the coherence length (≈ 1 μm), which is much smaller than the Rayleigh range in our experimental setup (≈ 100 μm). Consequently, the amplitude of the fundamental field may be removed from the phase matching integral. In the simplest case, if the laser is focused at a single dielectric–air interface at z_f and using the first term in Eq. (15), the time-dependent, amplitude-independent phase matching integral $J(\tilde{t})$ becomes

$$\tilde{J}(t) = \lim_{z_i \to -\infty} \int_{z_i}^{z_f} dz e^{-3\Gamma(t-\Delta\beta z)^2} e^{i\Delta k z} = -\sqrt{\frac{\pi}{\xi}} e^{(-\zeta_k^2 + 2i\zeta_k\zeta_t)} \mathrm{erf}\left[\zeta_t + \left(i\zeta_k - \frac{z_f \xi^{1/2}}{2}\right)\right]. \quad (16)$$

The scaling of the time-dependent radiated TH power (apart from unit factors)

$$\mathcal{P}_3(t) = |\tilde{f}_1^3 \rfloor_{z_f} \chi^{(3)} \tilde{J}(t)|^2 \quad (17)$$

is determined by the cube of the fundamental intensity at the interface located at $z=z_f$. Modeling a z-scan becomes simpler, because the integral in Eq. (16) is the same for every focal position and the interface contribution at $z=z_f$ is stated explicitly.

More generally, the TH response of multiple interfaces can be modeled. In Sec. IV, the TH response of a pulsed plane wave due to a finite optical element with a beginning and end at z_i and z_f was calculated. The solution, Eq. (13), has two terms. Each term describes TH originating at each interface. The sign differs, since the terms arise from an evaluation of the indefinite form of the integral in Eqs. (11) and (16). The time-dependent TH power for the two interfaces of a single slab on nonlinear material is

$$\mathcal{P}_3(t) \propto \left| \chi^{(3)} \sqrt{\frac{\pi}{\xi}} e^{(-\zeta_k^2 + 2i\zeta_k\zeta_t)} \times \left\{ \tilde{f}_1^3 \rfloor_{z_i} \mathrm{erf}\left[\zeta_t + \left(i\zeta_k - \frac{z_i \xi^{1/2}}{2}\right)\right] - \tilde{f}_1^3 \rfloor_{z_f} \ \mathrm{erf}\left[\zeta_t + \left(i\zeta_k - \frac{z_f \xi^{1/2}}{2}\right)\right] \right\} \right|^2. \quad (18)$$

Evaluating the amplitude of the fundamental field $\tilde{f}_1$ at each interfaces determines the relative contribution of each interface to the measured TH signal. Equation (18) can be applied to third-harmonic generation from any sized material, as long as the group walk-off length is much smaller than the Rayleigh range. The mathematical requirement is that $(\Delta\beta z_r \sqrt{\Gamma})^{-1} \gg 1$.

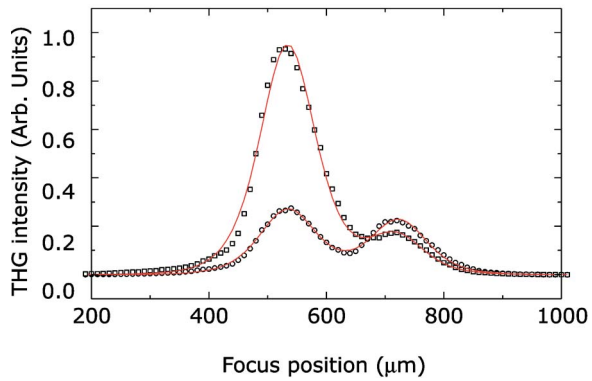

FIG. 7. (Color online) z-scan data from the AlN–sapphire and bare substrate samples and fitted curves. The top curve (□) is from the film and substrate, and the lower curve (○) is from the bare substrate. I_b and I_m denote the measured substrate and substrate and film intensities at $z_0=540$ μm. The horizontal axis is the laboratory-coordinate distance the sample was moved. Within the sapphire, the focus moves across a larger distance, scaled by $n_1=1.76$.

B. Application to thin-film $\chi^{(3)}$ measurements

Determining the value of $\chi^{(3)}_{\mathrm{AlN}}$ requires deconvoluting the TH response of the AlN film and the Al_2O_3 substrate. The experimental requirement is manifold. One must measure the TH response of the substrate and the TH response of the AlN-coated substrate, as well as the linear optical parameters of both the film and sapphire substrate. The linear optical properties of AlN were determined through the use of an optical parameter extraction (OPE) calculation in Sec. III. The linear thickness was also determined to be 0.31(1) μm. The phase matching and inverse group velocity are listed in Table IV and are the primary variables used for modeling THG in a thin film on a substrate; however, we included the Fresnel coefficients in Table II, to obtain the most accurate estimate for $\chi^{(3)}$.

Both the bare and coated substrates were measured using the third-harmonic z-scan technique [7]. To satisfy the requirement for the interface model the (vacuum) Rayleigh range of the laser focus was approximately 200 μm, which is greater than the walk-off length in the sapphire substrate ($\approx$25 μm), determined by the damping distance of the Maker fringes in Fig. 3. The experimental data are shown in Fig. 7. Because the electric field near each interface is approximately independent of z, it can be factored out of the phase matching integrals for each of the air–AlN, and AlN–sapphire interfaces. Consequently, the shape of the z-scan measurements shown in Fig. 7 described by a sum of cubed Lorentzians:

$$\mathcal{P}_{3\omega}(z)=\left[\frac{a_0}{1+[(z-z_0)/z_r]^2}\right]^3+\left[\frac{a_1}{1+[(z-z_1)/z_r]^2}\right]^3, \tag{19}$$

where $z_1=z_0+L$. The fitting parameters are listed in Table V.

The data are presented in the laboratory-frame translation units, and the fit allowed us to determine several optical parameters. Taking the average of measurements derived for the coated and bare substrate, we determined the substrate optical thickness L to be 187 μm. Multiplying L by $n_1=1.76$ indicated a physical thickness of 328 μm. The Rayleigh range z_r was also found from the Lorentzian fit. The value 111 μm corresponds to the value of z_r within the sapphire and is consistent with a focal waist diameter of 15 μm.

Knowing the relative signals I_b (substrate) and I_m (substrate–film) is required for calculating the film's susceptibility. In the sequential measurements of the coated and bare samples, the signal due to the interface at 710 μm is different, because the reflection coefficient at the second interface. The measured values are scaled by the square of the relative Fresnel factors $|\mathcal{F}_3^{\mathcal{B}}/\mathcal{F}_3^{\mathrm{TF}}|^2$ for the TH field propagating from the first interface, through the sample, to the detector. Including the Fresnel factor produces a pump-normalized relative intensity ratio of $I_m/I_b=3.53(4)$.

The measured energy densities I_m and I_b are related to the calculated fields through an inner product. The energy density of the ith TH field (aside from the factor of $\sqrt{\mu\epsilon}$) is computed with the time integral

$$I_i=\int_{-\infty}^{\infty}dt\tilde{A}_i(t)\tilde{A}_i^*(t). \tag{20}$$

The total field radiated from the Al_2O_3-AlN interface,

$$\tilde{A}_m(t)=\tilde{A}_f+\tilde{A}_b, \tag{21}$$

is the superposition of the substrate-generated field and the film-generated field, in which case,

$$I_m=\int_{-\infty}^{\infty}dt\tilde{A}_b(t)\tilde{A}_b^*(t)+\int_{-\infty}^{\infty}dt\tilde{A}_f(t)\tilde{A}_f^*(t)+\int_{-\infty}^{\infty}dt\tilde{A}_b(t)\tilde{A}_f^*(t)+\int_{-\infty}^{\infty}dt\tilde{A}_f(t)\tilde{A}_b^*(t) \tag{22}$$

and

$$I_b=\int_{-\infty}^{\infty}dt\tilde{A}_b(t)\tilde{A}_b^*(t). \tag{23}$$

Each TH field $\tilde{A}_i(t)$ is proportional to a susceptibility $\chi_i^{(3)}$ and phase matching factor $\tilde{J}_i(t)$, with the Fresnel reflection

TABLE V. Parameters from Lorentzian fit.

Sample	a_0 (arb units)	a_1 (arb units)	z_r (μm)	z_0 (μm)	L(μm)
Substrate	64.5(2)	60.8(2)	112.5(7)	534.3(4)	188.8(6)
AlN–substrate	98.2(3)	54.2(7)	110(1)	544.1(5)	184(3)

TABLE VI. C_i Parameters from phase matching integrals.

C_i	Definition[a]	Value (arb units)
C_1	$\lvert J_{\mathrm{AlN}}\rvert^2$	$(\mathcal{F}_1^B\mathcal{F}_1^{\mathrm{TF}})^6(\mathcal{F}_3^{\mathrm{TF}})^2\times 1.6(3)$
C_2	$\lvert J_{\mathrm{Al_2O_3}}\rvert^2$ (with coating)	$(\mathcal{F}_1^B)^6(\mathcal{F}_3^{\mathrm{TF}})^2\times 6.5$
C_3	$\int_{-\infty}^{\infty}dt(\tilde{J}_{\mathrm{AlN}}\tilde{J}^*_{\mathrm{Al_2O_3}}+\tilde{J}_{\mathrm{Al_2O_3}}\tilde{J}^*_{\mathrm{AlN}})$	$(\mathcal{F}_1^B)^6(\mathcal{F}_1^{\mathrm{TF}})^3(\mathcal{F}_3^{\mathrm{TF}})^2\times -4.3(6)$
C_4	$\lvert J_{\mathrm{Al_2O_3}}\rvert^2$(bare sapphire)	$(\mathcal{F}_1^B)^6(\mathcal{F}_3^B)^2\times 6.5$
$\chi^{(3)}_{\mathrm{AlN}}/\chi^{(3)}_{\mathrm{Al_2O_3}}$	Eq. (28) (including reflections)	7.7(8)

[a]Note that $\tilde{J}_{\mathrm{AlN}}$ incorporates both thin film interfaces, as in Eq. (18), and $\tilde{J}_{\mathrm{Al_2O_3}}(t)$ accounts for just one interface, as in Eq. (16). $\lvert J\rvert^2=\int_{-\infty}^{\infty}dt\tilde{J}(t)\tilde{J}^*(t)$.

and units constants absorbed into the phase matching integrals. Equation (22) can be rewritten as

$$I_m=\lvert\chi^{(3)}_{\mathrm{AlN}}\rvert^2\lvert J_{\mathrm{AlN}}\rvert^2+\lvert\chi^{(3)}_{\mathrm{Al_2O_3}}\rvert^2\lvert J_{\mathrm{Al_2O_3}}\rvert^2+\lvert\chi^{(3)}_{\mathrm{Al_2O_3}}\rvert\lvert\chi^{(3)}_{\mathrm{AlN}}\rvert\times\left(\int_{-\infty}^{\infty}dt\tilde{J}_{\mathrm{AlN}}(t)\tilde{J}^*_{\mathrm{Al_2O_3}}(t)+\tilde{J}_{\mathrm{Al_2O_3}}(t)\tilde{J}^*_{\mathrm{AlN}}(t)\right).\quad(24)$$

Both the phase and amplitude information of both the substrate harmonic field $\tilde{A}_b(t)$ and the film-generated field $\tilde{A}_f(t)$ were retained in the calculation. Cross terms were kept and evaluated. The integrals evaluated to four constants C_1, C_2, C_3, and C_4 and are defined in Table VI. Substituting these constants into Eq. (24) gives the simplified expression

$$I_m=\lvert\chi^{(3)}_{\mathrm{AlN}}\rvert^2C_1+\lvert\chi^{(3)}_{\mathrm{Al_2O_3}}\rvert^2C_2+\lvert\chi^{(3)}_{\mathrm{Al_2O_3}}\rvert\lvert\chi^{(3)}_{\mathrm{AlN}}\rvert C_3.\quad(25)$$

Dividing Eq. (25) by

$$I_b=\lvert\chi^{(3)}_{\mathrm{Al_2O_3}}\rvert^2C_4\quad(26)$$

reduces the problem to solving the quadratic equation

$$\left(\frac{\chi^{(3)}_{\mathrm{AlN}}}{\chi^{(3)}_{\mathrm{Al_2O_3}}}\right)^2\frac{C_1}{C_4}+\left(\frac{\chi^{(3)}_{\mathrm{AlN}}}{\chi^{(3)}_{\mathrm{Al_2O_3}}}\right)\frac{C_3}{C_4}+\left(\frac{C_2}{C_4}-\frac{I_m}{I_b}\right)=0.\quad(27)$$

It has the solution

$$\frac{\chi^{(3)}_{\mathrm{AlN}}}{\chi^{(3)}_{\mathrm{Al_2O_3}}}=\frac{-C_3/C_4\pm\sqrt{(C_3/C_4)^2-4(C_1/C_4)[C_2/C_4-(I_m/I_b)]}}{2(C_1/C_4)}.\quad(28)$$

First, Eq. (28) was evaluated assuming no reflective losses, which amounts to using the values in Table VI, with the $\mathcal{F}_i^j=1$. Making the substitutions and taking the positive root indicates the ratio $\chi^{(3)}_{\mathrm{AlN}}/\chi^{(3)}_{\mathrm{Al_2O_3}}$ is 4.82. Then, we factored in all the reflections listed in Table VI as they are given in Table II and found a reflection-corrected value for the susceptibility ratio, 7.7(8).

If the value of the sapphire susceptibility is known, it can be used to estimate the magnitude of $\chi^{(3)}_{\mathrm{AlN}}$. The rotational symmetry of the substrate TH measurement in Fig. 2 allows for the film and sapphire tensors to be approximated as isotropic. It can be assumed that for some measured angle, the fundamental field polarization was aligned with the x axis of the sapphire. At that position, the only nonzero tensor element is $\chi^{(3)}_{xxxx}$. The known value of the tensor component $\chi^{(3)}_{xxxx}$ for sapphire, $1.14\pm0.15\times10^{-14}$ esu was corrected for wavelength and used to determine the susceptibility of aluminum nitride $1.52\pm0.25\times10^{-13}$ esu[2]. In computing the error on the film to substrate $\chi^{(3)}$ ratio, we only considered the error in the AlN film C_1 and C_3 parameters.

VI. THG SPECTRUM

For each z-scan focus position, the TH signal propagated through a monochrometer and the spatially dispersed TH spectrum was imaged on an intensified silicon diode array (Optical Multichannel Analyzer, Princeton Inst. Model 1420). Closing the entrance slit allowed just the forward-propagating beam to enter and produced a TH spectrum containing a significant amount of structure. As mentioned in the context of the disappearance of Maker fringes in ultrafast experiments, the sensitivity to the material thickness is maintained by the relative phase of two pulses generated at the entrance and exit interfaces of the sapphire substrate. The TH phase is observable when the TH field is spectrally resolved. In the experiments, we observed a relationship between the spectral oscillations and the laser focus position. The spectrally resolved data are shown in Fig. 8. They are displayed separately to eliminate overlapping and are labeled according to the location of the laser focus.

The spectral modulation is clearest in the data taken while focusing near the air–sapphire interface. There, the centroid is also well defined and constant over a large range of focus positions. We chose to analyze the spectrum at $z_0=680$, because it has the best fringe-to-height contrast, since the TH pulse from the AlN–Al_2O_3 interface and the TH pulse from the air–Al_2O_3 interface are nearly equal in amplitude. The spectral data taken when focusing near the AlN–air interface show some distortion, because of the angular spread of **k** vectors in the beam.

[2]We calculated $\chi^{(3)}_{\mathrm{THG}}$ of sapphire from known DFWM measurement by Levenson. Assuming a sapphire band gap $\lambda'=150$ nm, the ratio $\lambda/\lambda'=5.3$ implies the ratio of the susceptibilities, $\chi^{(3)}_{\mathrm{THG}}/\chi^{(3)}_{\mathrm{DFWM}}=\lambda^3(1-5.3)^3/[\lambda^3(1-5.3)(2-5.3)(3-5.3)]=2.41$ at $\lambda=800$ nm. Similarly, $\chi^{(3)}_{\mathrm{DFWM}}(800\ \mathrm{nm})/\chi^{(3)}_{\mathrm{DFWM}}(550\ \mathrm{nm})=0.72$. Multiplying the known value 1.14×10^{-14} esu by the previous values determines $\chi^{(3)}_{\mathrm{THG}}=1.97\times10^{-14}$ esu at 800 nm. As a comparison, we repeated the derivation using Miller's rule, and found a slightly lower TH susceptibility for sapphire $\chi^{(3)}_{\mathrm{THG}}=1.37\times10^{-14}$ esu [37].

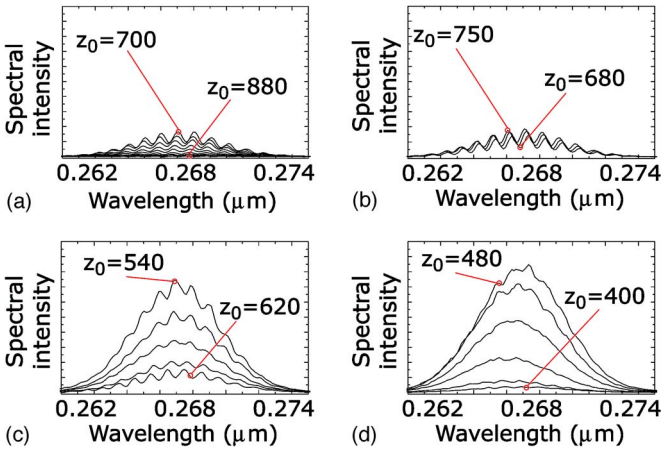

FIG. 8. (Color online) Spectrally resolved z-scan data of AlN-coated sapphire. Each curve corresponds to a different focus position z_0.

A. Fourier analysis

Multiple TH pulses will interfere in the detector if the thickness of the material is comparable to the Rayleigh range of the laser focus [7]. Figure 8 demonstrates that the effect is sustained in our AlN sample. The interference has several properties which can be used to characterize the material. The spectral intensity

$$|\tilde{A}_3(\omega)|^2 = (2\pi)^{-1}\left|\int_{-\infty}^{\infty} dt \tilde{A}_3(t) e^{i\omega t}\right|^2 \tag{29}$$

is the absolute value squared of the Fourier transform of the approximate time-dependent TH field,

$$\tilde{A}_3(t) = (e^{i\Phi_1} e^{-3\Gamma(t-\tau/2)^2} + e^{i\Phi_2} e^{-3\Gamma(t+\tau/2)^2}). \tag{30}$$

The analytical evaluation of the integral of Eq. (29) gives

$$|\tilde{A}_3(\omega)|^2 = \left| \frac{e^{-\omega(6i\Gamma\tau+\omega)/12\Gamma}}{\sqrt{6\Gamma}} (e^{i\Delta\Phi} + e^{i\tau\omega}) \right|^2, \tag{31}$$

or in units of wavelength, it evaluates to

$$|\tilde{A}_3(\lambda)|^2 \propto e^{(2^2c^2\pi^2/6\Gamma)(1/\lambda - 1/\lambda_0)^2} \cos^2\left[\left(\frac{\pi c\tau}{\lambda}\right) - \Delta\Phi\right], \tag{32}$$

where the TH centroid $\lambda_0 = \frac{2\pi}{\omega_0}$ and the constant phase factor $\Delta\Phi = \Phi_2 - \Phi_1$.

The phase $\Delta\Phi$ was used to fit the constant phase difference between the two pulses. We neglected the linear term, corresponding to a pulse chirp difference, since it is nearly zero, as shown in Fig. 6. If included, this linear term will cause the envelope of the power spectrum to shift, because the terms proportional to t can be absorbed into the complex exponential.

The relative phase of the two pulses determines the position of the spectral oscillations. For an unfocused beam, the spectral phase is only related to the thickness of the nonlinear material, as mentioned in the discussion of Fig. 3. However, focusing introduces additional phase. We modeled the focus dependence of $\Delta\Phi$ using the analytical solution in Eq. (18) and additional shifts from focusing. We mapped the predicted phase offset as the focus scans through the sample, but found that it does not match the observed shift of the phase in Fig. 8. The deviation of the experimental data is caused by spatial far-field coherence not included in the paraxial approximation of THG. In addition to the relative phase dependence on focus position, anomalous spectral behavior appeared when the focus was placed near the AlN interface, shown in Fig. 8(d), which is not explained by any of the analysis in the previous sections.

TABLE VII. Parameters from THG spectral fit.

Parameter	Value	Units
Γ	0.00140(6)	fs^{-2}
τ	232.07(3)	fs
$\Delta\Phi$	1.98(2)	rad
$\lambda_0/3$	0.26699(5)	μm

The spectrum was fit (see Table VII) using Eq. (32) and the result is plotted in Fig. 9. The value of Γ determined by the spectral fit [0.001 40(6)] agrees well with the expected value in Table III (0.001 41), obtained from measurements of the fundamental bandwidth. The fitted time separation of the pulses, τ=232.07, is more accurate than estimates from published data on sapphire (260 fs). A more accurate value for the inverse group velocity mismatch $\Delta\beta = L/\tau = 0.70(5)$ fs μm^{-1} is found by using the measured Γ value along with the substrate thickness data in Table V. However, the improved value for Γ only corrects the calculated film to substrate susceptibility ratio $\chi^{(3)}_{AlN}/\chi^{(3)}_{Al_2O_3}$ by 0.02%. On the other hand, a change of equal magnitude (10%) in the value of Δk for Al_2O_3, when evaluated with Eq. (28), produced a 10% correction.

B. Nonparaxial effects

Closing the entrance slit to the monochrometer was required to reveal the TH spectral oscillations, but produced a

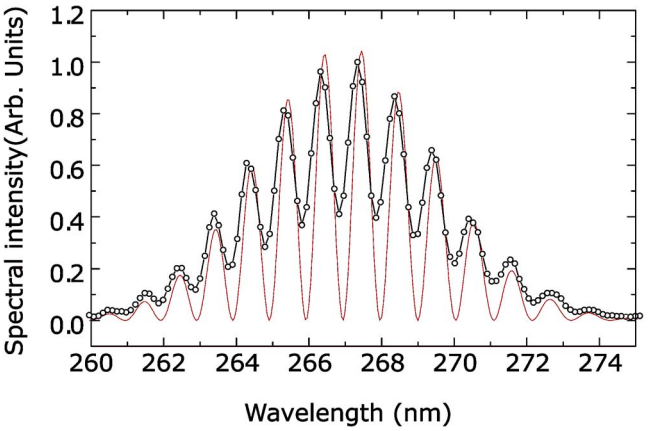

FIG. 9. (Color online) Least-squares fit of TH signal(◦) fitted using the transform model in Eq. (32). The parameters for the fit are shown in Table VII. The experimental data correspond to the lowest TH signal in Fig. 8(b).

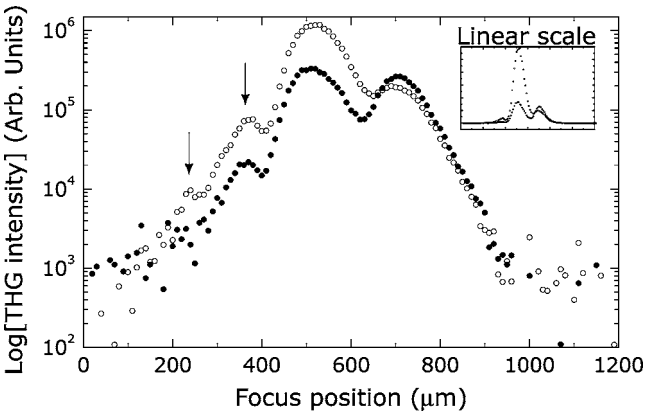

FIG. 10. Measured TH z-scans of the AlN sample and bare substrate, with a nearly closed entrance slit to the spectrometer. An asymmetric line structure is observed and additional peaks (arrows) appear when the focus is placed on the spectrometer side of the sample. Both the sapphire substrate (•) and the AlN-coated sapphire (◦) exhibit this effect. In each case, the extra peak intensities scale linearly with the interface signal.

significantly different shape of the z-scan curve compared to Fig. 7. z-scan measurements of the same sample measured in Sec. V, except under spectrally resolving conditions, are shown in Fig. 10. In general, the shape of the z-scan data was less symmetric when the slit was closed. We also observed oscillations in the intensity over a small range of focus positions. The new features in the z-scan data observed under spectrally resolving conditions correlate with the anomalous spectra in Figs. 8(c) and 8(d). To account for nonparaxial THG, a geometric factor that relates the forward-generated TH to the spread in **k** vectors of the focused pump is required [16,22,34,35].

VII. CONCLUSIONS

We presented several measurements of an AlN film grown on sapphire, which were combined and used to determine the nonlinear susceptibility $\chi^{(3)}$ of the AlN film. A rigorous model for scanning laser (z-scan) third-harmonic generation that relied on ultrafast effects was developed and was used to model the shape of the z-scan. Interface sensitivity arising from ultrafast effects were exploited to avoid including long-range coherence related to Gaussian focusing. Overall, it afforded a simple, analytical description of interface THG measurements under the generally applicable phase mismatched condition, as long as the Rayleigh range is long compared to group velocity walk-off length.

The rotational measurements of the textured AlN film showed a strong second-harmonic dependence, but did not indicate any rotational anisotropy in the third harmonic. Analysis of the SH rotational anisotropy showed the AlN texture is nearly wurzite, but the z-axis of the film is slightly tilted with respect to the z-axis of the substrate[3]. We compared the TH rotational measurement of AlN to a z-cut quartz crystal, which displayed the rotational dependence expected from bulk THG. Because neither the thin film nor the substrate shows any rotational anisotropy in THG, it is likely that the spread in **k** vectors in a tightly focused pump laser reduces the resolution of the tensor components. That being the case, more accurate rotational measurements would be available when using a collimated, amplified laser system.

We deconvolved the response of the film from the measured TH from the film on the substrate using the time-domain interference model. Calculations of the time-dependent amplitude and phase of the fields in two adjacent slabs of nonlinear material showed that the amplitude of the TH field contains a sequence of pulses, each of which corresponds to a material interface. Using the z-scan technique allowed for the critical thin-film interface to be isolated. From our experiments, we determined the film-to-substrate susceptibility ratio $\chi^{(3)}_{\mathrm{AlN}}/\chi^{(3)}_{\mathrm{Al_2O_3}}=7.7(8)$. Using previously published data for sapphire, we concluded that $\chi^{(3)}_{xxxx}(\mathrm{AlN})=1.52\pm0.25\times10^{-13}$ esu.

The emitted interface pulses also contain information regarding the bulk of the material, but it is contained in the relative phase of each pulse. For ultrashort-pulse measurements in bulk materials which are thicker than the group velocity walk-off length, measuring the relative phase of the emitted pulse pair is equivalent to measuring Maker fringes in a cw experiment. By spectrally resolving the TH field, we used the ultrafast model to measure the relative phase of the pulses generated at the air–sapphire and sapphire–AlN interfaces and showed we could retain the information contained in Maker fringes.

Though the time-domain analysis showed that interfaces produce the TH field, it fails to describe why interfaces are so important for generating the harmonics. More insight may be gained by considering harmonic generation and pulse propagation in terms of adiabatic versus nonadiabatic interactions with a material. In this context, interfaces introduce a nonadiabatic disturbance during pulse propagation, but within the bulk of the material the fundamental pulse propagates adiabatically. Our approximation assumed that the instantaneous bulk TH polarization does not interact with the interface field, because such a long-range coherence is removed when the group velocity walk-off length is short compared to the Rayleigh range.

The spectral analysis indicated that ultrafast third-harmonic generation is a promising phase-sensitive diagnostic. To record the spectral phase we used a smaller numerical aperture (NA) lens than has been reported in the THG microscopy literature. A lower NA makes our setup inferior as an imaging system, but affords an interferometric measurement by generating multiple pulses from macroscopically spaced interfaces in the sample. A previous experiment by Banfi *et al.* showed that multiple pulses originate from interfaces in a bulk sample, but chose to separate the pulses for use in timing experiments, rather than allow them to interfere spectrally [23]. If the group-velocity mismatch in the substrate is known accurately, the spectral phase can be used to record small changes in the thickness of a thin film, as well as other phase shifts due to imaginary components of a

[3]The texture fit is insensitive to tilts less than 20°; independent rocking x-ray measurements indicate a tilt of 2° [9].

susceptibility tensor. Even with our choice of a lower NA lens, we observed that the nonparaxial interaction with the samples distorted both the amplitude and phase of the TH field for several laser focus positions. To improve the accuracy of the pulse phase measurement for all focus positions, the effect of a nonparaxial beam should be included.

ACKNOWLEDGMENTS

Thanks to R. Carilles and Y. Q. An for their expert advice and loan of experimental equipment and to B. Breizman for helpful discussions. This research was supported by NSF Grant No. DMI-0304031 and received partial funding by the Robert A. Welch Foundation and SPRING.

[1] M. Sheik-Bahae, A. Said, and E. V. Stryland, Opt. Lett. **14**, 955 (1989).
[2] T. Y. F. Tsang, Phys. Rev. A **52**, 4116 (1995).
[3] T. Tsang, M. A. Krumbügel, K. W. DeLong, D. N. Fitinghoff, and R. Trebino, Opt. Lett. **52**, 1381 (1996).
[4] Y. Barad, H. Eisenberg, M. Horowitz, and Y. Silberberg, Appl. Phys. Lett. **70**, 922 (1997).
[5] R. Barille, L. Canioni, L. Sarger, and G. Rivoire, Phys. Rev. E **66**, 067602 (2002).
[6] P. N. Saeta and N. A. Miller, Appl. Phys. Lett. **79**, 2704 (2001).
[7] D. Stoker, M. C. Becker, and J. W. Keto, Phys. Rev. A **71**, 061802 (2005).
[8] L. P. Wang, D. S. Shim, Q. Ma, V. R. Ra, E. Ginsburg, and A. Talalyevsky, J. Vac. Sci. Technol. A **23**, 1284 (2005).
[9] J. Baek, J. Keto, M. Becker, and D. Kovar (unpublished).
[10] C. Ristoscu, E. Gyorgy, I. N. Mihailescu, A. Klini, V. Zorba, and C. Fotakis, Appl. Phys. A: Mater. Sci. Process. **79**, 927 (2004).
[11] N. A. Sanford, A. V. Davydov, D. V. Tsvetkov, A. V. Dmitriev, S. Keller, U. K. Mishra, S. P. DenBaars, S. S. Park, J. Y. Han, and R. J. Molnar, J. Appl. Phys. **97**, 053512 (2005).
[12] G. Petrov, V. Shcheslavskiy, V. V. Yakovlev, I. Ozerov, E. Chelnokov, and W. Marine, Appl. Phys. Lett. **83**, 3993 (2003).
[13] W. P. Lin, P. M. Lundquist, G. K. Wong, E. D. Rippert, and J. B. Ketterson, Appl. Phys. Lett. **63**, 2875 (1993).
[14] P. M. Lundquist, W. P. Lin, Z. Y. Xu, G. K. Wong, E. D. Rippert, J. A. Helfrich, and J. B. Ketterson, Appl. Phys. Lett. **65**, 1085 (1994).
[15] T. Suga, S. Kameyama, S. Yoshioka, T. Yamamoto, and I. Tanaka, Appl. Phys. Lett. **86**, 163113 (2005).
[16] J. Xin Cheng, A. Volkmer, L. D. Book, and X. S. Xie, J. Raman Spectrosc. **34**, 642 (2003).
[17] C.-K. Sun, S.-W. Chu, S.-P. Tai, S. Keller, U. K. Mishra, and S. P. DenBaars, Appl. Phys. Lett. **77**, 2331 (2005).
[18] D. Debarre, W. Supatto, and E. Beaurepaire, Opt. Lett. **30**, 2134 (2005).
[19] J. F. Ward and G. H. C. New, Phys. Rev. **185**, 57 (1969).
[20] G. C. Bjorklund, IEEE J. Quantum Electron. **QE-11**, 287 (1975).
[21] P. N. Saeta and N. A. Miller, Nature (London) **337**, 519 (1989).
[22] D. A. Kleinman and R. C. Miller, Phys. Rev. **148**, 302 (1966).
[23] G. P. Banfi, G. Ferrini, D. Finarelli, M. Peloi, and F. Parmigiani, Phys. Rev. A **64**, 063812 (2001).
[24] J. Miragliotta and D. K. Wickenden, Phys. Rev. B **50**, 14960 (1994).
[25] R. S. Tasgal and Y. B. Band, Phys. Rev. A **70**, 053810 (2004).
[26] A. E. Siegman, *Lasers* (University Science Books, Sausalito, 1986).
[27] R. C. Eckardt and J. Reintjes, IEEE J. Quantum Electron. **QE-20**, 1178 (1984).
[28] W. E. Angerer, N. Yang, A. G. Yodh, M. A. Khan, and C. J. Sun, Phys. Rev. B **59**, 2932 (1999).
[29] R. S. Tasgal, M. Trippenbach, M. Matuszewski, and Y. B. Band, Phys. Rev. A **69**, 013809 (2004).
[30] J. Baek, D. Kovar, J. W. Keto, and M. F. Becker, J. Appl. Phys. (to be published).
[31] W. K. Burns and N. Bloembergen, Phys. Rev. B **4**, 3437 (1971).
[32] R. B. Miles and S. E. Harris, IEEE J. Quantum Electron. **9**, 470 (1973).
[33] P. D. Maker, R. W. Terhune, M. Nisenoff, and C. M. Savage, Phys. Rev. Lett. **8**, 21 (1962).
[34] G. E. Francois and A. E. Siegman, Phys. Rev. **139**, A4 (1965).
[35] K. D. Moll, D. Homoelle, A. L. Gaeta, and R. W. Boyd, Phys. Rev. Lett. **88**, 153901 (2002).
[36] D. S. Stoker, Ph.D. thesis, The University of Texas at Austin, 2006.
[37] M. Levenson, IEEE J. Quantum Electron. **QE-10**, 110 (1974).